Edinburgh Research Explorer

Numerical simulation of vibration of horizontal cylinder induced by progressive waves

Numerical simulation of vibration of horizontal cylinder induced by progressive waves

Ming-Jyh CHERN[1], **E A Odhiambo**[1]‡, **Tzyy-Leng HORNG**[2] **and A G L Borthwick**[3]

[1]Department of Mechanical Engineering, National Taiwan University of Science and Technology, 43 Sec. 4 Keelung Road, Taipei 10607, Taiwan
[2]Department of Applied Mathematics, Feng Chia University, Taichung 40724, Taiwan
[3]School of Engineering, University of Edinburgh, Edinburgh, United Kingdom

E-mail: `mjchern.ntust@gmail.com`

Abstract. Maritime structures often comprise cylinders of small diameter relative to the prevailing wave length. This paper describes the Direct Forcing Immersed Boundary (DFIB) simulation of the hydroelastic behaviour of a rigid, horizontal circular cylinder in regular progressive waves. Fluid motions are numerically solved by the full Navier-Stokes equations, and the free surface by the Volume-of-Fluid (VoF) method. The Reynolds number Re = 110, Keulegan-Carpenter number KC = 10, Froude number Fr = 0.69 and Ursell number $U_{\text{rs}} \approx 12$. A single-degree-of-freedom model is used for the elastically mounted cylinder. Velocity profiles for the stationary cylinder case have been successfully validated using experimental results. The frequency response for reduced velocities $4.5 < U_R^* < 5.3$ have been compared with theoretical data. Three transverse vibration regimes are identified: lower beating $(4 < U_R^* < 4.5)$; lock-in $(4.7 < U_R^* < 4.8)$; and upper beating $(5 < U_R^* < 10)$ modes. The lower and upper beating regimes exhibit varying amplitude response. The lock-in mode represents the region of fixed and maximum response. The lower beating and lock-in modes have peaks at a common vibration to wave frequency ratio $f_w^* = 2$. For the upper beating mode, $f_w^* = 1$, except for $U_R^* = 10$ when $f_w^* = 2$.

‡ Corresponding author: d10203801@mail.ntust.edu.tw

Nomenclature

A	:	maximum amplitude of vibration (m)
c	:	damping coefficient (Ns/m)
C_f	:	in-line force coefficient
C_l	:	transverse force coefficient
D	:	diameter of cylinder (m)
d	:	water depth (m)
f_n	:	natural frequency of solid (Hz)
f	:	force coefficient and response frequency (Hz)
f_w	:	fundamental frequency of wave (Hz)
$\mathbf{f}$	:	virtual force per unit mass (N/kg)
$\mathbf{F}$	:	total virtual force (N)
Fr	:	Froude number, $U_m/\sqrt{gD}$
$\mathbf{g}$	:	gravitational acceleration (m/s^2)
h	:	cylinder depth (m)
H	:	wave height (m)
k	:	stiffness constant (N/m)
KC	:	Keulegan-Carpenter number, $U_m T/D$
L	:	domain length (m)
m_s	:	mass of solid (kg)
m	:	time step
n	:	phase step
$\mathbf{n}$	:	normal direction vector
N	:	number of sub-grid cells
p	:	pressure (Pa)
R	:	radius of cylinder (m)
Re	:	Reynolds number, $U_m D/\nu$
S	:	free surface profile
t	:	time (s)
T	:	period of oscillating flow (s)
$\mathbf{u}(u,v)$	:	fluid velocity (m/s)
$\mathbf{u}_s$	:	solid velocity vector (m/s)
$\mathbf{x}_s$	:	solid response vector (m)
U_{m}	:	amplitude of horizontal wave velocity (m/s)
U_R^*	:	reduced velocity, $U_m/f_n D$
U_{rs}	:	Ursell number, $H\lambda^2/d^3$
x, y	:	Cartesian coordinates (m)

Greek Symbols

α	:	volume of fluid fraction
ϵ	:	ratio of distance between neighbouring cells on free surface to
	:	distance between wet cell to free surface
γ	:	surface elevation (m)
κ	:	wave number (rad/m)
λ	:	wavelength (m)
Φ	:	relaxation parameter
Ψ	:	generalized field values
ω	:	wave frequency (rad/s)
Ω	:	domain
ρ	:	fluid density (kg/m^3)
ξ	:	sub-grid indicator function
ζ	:	damping ratio
η	:	the volume of solid function
ν	:	kinematic viscosity of fluid (m^2/s)

Subscripts

ab	:	absorption zone
ac	:	artificial compression
an	:	analytical values
c	:	cylinder centre
cp	:	computational values
gen	:	generation zone
i, j, k, l	:	numerical cell indices
o	:	atmospheric
s	:	solid
rms	:	root mean square

Superscripts

d	:	dry
m	:	time level
w	:	wet
$*$	:	dimensionless quantity
$**$	:	intermediate time level

1. Introduction

Offshore structures typically comprise single or multiple column installations. In relatively shallow waters, oil and gas platforms may be constructed as fixed jackets with marine risers connecting into the superstructure at deck level. Such structures are usually fabricated using circular cylinders that are of much smaller diameter than the wavelength of the prevailing ocean waves. Offshore wind turbines may be sited on single column structures. Marine aquaculture farms, piers, jetties, and maritime navigation facilities can also have multi-cylinder support structures. There are also novel tidal stream and wave energy devices, designed to exploit cylinder responses in waves.

Small diameter cylinders are bluff bodies that promote flow separation, and the shedding of vortices/eddies to form wakes. Vortical flow structures that detach from a cylinder may be either sustained or attenuated depending on the balance between energy extracted from the free stream across the wake shear layers and the dissipated energy through turbulence and molecular diffusion. For hydroelastic cylinders, sustained vortical action may be accompanied by cyclic hydrodynamic loadings and responses, leading to vortex-induced-vibration (VIV), which itself may be constructive or destructive. Efforts to suppress vortex-induced vibration are relevant to the structural integrity of offshore installations, whereas resonant responses of cylinders may be beneficial in the context of renewable energy devices. Of particular interest to offshore engineers is the amplitude response behaviour of cylinders in operating and extreme sea states where the wave elevations cover a range of frequencies and amplitudes.

Many studies have investigated the fluid-structure interaction (FSI) of structures immersed in regular progressive waves. In the 1970s, a group of researchers at Bristol University began to exploit the wave energy harvesting potential of FSI for a submerged horizontal cylinder in waves, which was mounted on spring supports. Evans et al. (1979) reported findings from these laboratory tests which demonstrated that a submerged circular cylinder could be quite efficient in absorbing energy from a regular wave train. In a study related to the vibrations of structural elements in offshore platform substructures, Borthwick and Herbert (1990) explored the resonant and non-resonant behaviour of a spring-mounted vertical cylinder in waves using a laboratory flume, and established that peak values of force coefficients and response amplitudes occurred when the ratio of wave frequency to cylinder natural frequency in water was an integer submultiple. Koji and Yoshiho (1996) visualized the flow patterns in the vicinity of a stationary horizontal cylinder at low Keulegan-Carpenter (KC) numbers (where $KC = U_m T/D$, with U_m being the amplitude of the sinusoidal undisturbed flow velocity, T the oscillation period, and D the diameter of the cylinder), the aim being to ascertain the loading mechanism due to circulation. Koji and Yoshiho compared their experimental measurements of vortex shedding patterns in regular waves against corresponding patterns in planar oscillatory flows obtained by Sawamoto and Kikuchi (1979). The orbital motion of vortices attached to the cylinder in regular waves was found to contrast with the planar oscillatory flow patterns, which involved non-orbiting

vortices that simply swept to and fro across the cylinder. Beji and Battjes (1993) carried out a laboratory investigation of wave propagation past a trapezoidal obstacle. Spectral analysis confirmed the presence of high frequency energetic motions, attributable to FSI. By considering the effect of the flow free surface on the vorticity concentration around a horizontal circular cylinder, Oshkai and Rockwell (1999) showed that proximity of the free surface could alter the vorticity dynamics. Mouazé and Bélorgey (2003) determined experimentally the effect of a solid bed boundary on the dynamics of a horizontal cylinder in waves, and observed that the flow tended towards planar oscillatory motions the closer the cylinder was to the bed. Other researchers, including Sarpkaya (1976), Kaye and Maull (1993), Sumer and Fredsøe (1988), Longoria et al. (1991), Yang and Rockwell (2004) and Han et al. (2015) have also studied the dynamic behaviour of (mainly) vertical cylinders in oscillatory flows.

Numerical modelling of fluid-structure interaction has gradually become more achievable as computer performance has improved and computational fluid dynamics (CFD) has matured. Despite the limited computational capacity at the time, Hideaki and Young-Gill (1990) simulated vortex motions in the vicinity of a horizontal cylinder using a finite-difference solver of the governing equations. According to Hideaki and Young-Gill the interactions between vortices grew more complicated in cases within the range, $1 < KC < 3$. Hideaki and Young-Gill also successfully validated the model calculations of the pressure distribution on the surface of the cylinder. Armenio (1998) presented results from the hydrodynamic analysis for a submerged body in a numerical wave tank. Armenio used an improved version of the free surface marker and cell (MAC) algorithm, known as semi-implicit marker and cell (SIMAC), to assess the effects of vortex generation and shedding on the inertia force. Shen and Chan (2008) used a variant of the immersed boundary method coupled with the volume-of-fluid (VoF) method to examine the reliability of non-body conforming mesh generation schemes in the context of FSI. Park et al. (2010) commented on the difficulties encountered in model validation when a current was also included in a numerical wave flume. Park et al. found satisfactory agreement between their results for progressive wave loading on a cylindrical platform structure and estimates calculated using the empirical design equation due to Morison et al. (1950). Choi et al. (2010) demonstrated the capability of a curvilinear non-hydrostatic model to simulate wave dispersion, diffraction, and reflection due to curved sidewalls. More recently, Canan and Serpil (2014) numerically investigated the interaction of free surface waves with an oscillating cylinder, and reported the occurrence of two new locked-on states of vortex formation in the near wake of the cylinder.

Traditionally planar oscillatory flow has been used to mimic the effect of waves on structures. The drawback with this approach is that the effect of the free surface is not captured. Furthermore, real waves have orbital motion, unlike the purely reversing motion of plane oscillatory flows.

This paper describes a numerical wave tank (NWT) used to study the interaction between regular, viscous, free surface gravity waves and a horizontally mounted cylinder. The model cylinder is permitted to undergo response motions in the vertical direction,

by means of a spring of stiffness k in accordance with a single-degree-of-freedom (SDOF) system (Chakrabarti and Cotter, 1978), and, depending on the damping, will respond to the hydrodynamic loading due to vortex shedding. A combination of VoF and direct forcing immersed boundary (DFIB) methods is used to model wave loading on the submerged cylinder as it responds. The cylinder is located in shallow water in the proximity of a solid bed. The DFIB method is based on a fixed Cartesian mesh framework, with a non-slip boundary imposed by a forcing function on the fluid-solid interface. By being able to handle a moving flow-structure domain (Ω_s) on a fixed mesh, the DFIB method effectively shifts the challenge of modelling FSI cases from mesh generation to the flow solver, through inclusion of a direct forcing function in the Navier-Stokes equations. Use of a sub-grid Cartesian mesh to capture a sharper fluid-solid interface marks an improvement on the earlier version of mesh used by Noor et al. (2009). The paper also provides evidence that use of OpenFOAM© together with parallel programming based on MPIRUN can reduce the computational runtime by up to 30%.

2. Mathematical Description

For fluid flow, the governing equations are given for mass conservation by

$$\frac{\partial \rho}{\partial t} + \nabla \cdot (\rho \mathbf{u}) = 0 \tag{1}$$

and momentum conservation by the Navier-Stokes equation,

$$\frac{\partial (\rho \mathbf{u})}{\partial t} + \nabla \cdot (\rho \mathbf{u}\mathbf{u}) = -\nabla p + \mu \nabla^2 \mathbf{u} + \rho \mathbf{g} + \rho \mathbf{f} \tag{2}$$

where ρ is the fluid density, $\mathbf{u}$ is the velocity vector, p is the pressure, t is time, ∇ is the gradient vector, μ is the dynamic viscosity coefficient of the fluid, $\mathbf{g}$ is the acceleration due to gravity, and $\mathbf{f}$ is the virtual force vector.

Figure 1 provides a definition sketch of the problem setup in two-dimensions: in the horizontal x-direction aligned with the incident wave direction; and y in the vertical direction. The Cartesian axes have their origin at the still water level (SWL) intersection with the left hand end of the domain. The figure shows a horizontal circular cylinder of mass m whose centre is located at (x_c, y_c), suspended from a spring of constant stiffness, k, with a dashpot damper, c, such that it is constrained to be a lumped parameter SDOF system able to respond in the vertical (transverse) y-direction only. A Lagrangian approach is used to trace the path taken by the rigid horizontal cylinder, with the elevation of the mid-point of the cylinder, y_c, determined from its equation of motion,

$$m_s \ddot{y}_c + c \dot{y}_c + k y_c = F_y \tag{3}$$

where F_y is the transverse (vertical) component of the total hydrodynamic force,

$$\mathbf{F} = \int_{\Omega_s} \rho \mathbf{f}^m(x, y) \mathrm{d}\forall. \tag{4}$$

The horizontal cylinder is initially at rest, and so the initial condition for the equation of motion is:

$$y = 0, \dot{y} = 0, t = 0.$$

Inline (C_f) and lift (C_l) coefficients are obtained from

$$C_f = \frac{F_x}{\frac{1}{2}\rho D U_\mathrm{m}^2} \tag{5}$$

$$C_l = \frac{F_y}{\frac{1}{2}\rho D U_\mathrm{m}^2} \tag{6}$$

where D is the cylinder diameter and U_m is the amplitude of the horizontal wave velocity component at elevation $y = y_c$.

We now consider the model boundary conditions. Following (Jacobsen et al., 2012), the NWT comprises three main regions, namely the wave generation, the computational and absorption zones (as indicated in figure 1).

Linear progressive waves are prescribed at the left hand, wave generator boundary at x = 0. Here, the wave particle horizontal velocity time series is prescribed according to small amplitude linear (Airy) wave theory (Dean and Dalrymple, 1984) using a shallow water approximation as follows

$$u(0,\mathrm{t}) = U_\mathrm{m}\cos(\omega t) \tag{7}$$

where the maximum horizontal wave particle velocity is obtained from

$$U_\mathrm{m} = \sqrt{\frac{\mathbf{g}}{d}\frac{H}{2}}. \tag{8}$$

and u is the horizontal water particle velocity, H is the wave height, ω is the wave angular frequency, and d represents the water depth.

At $x = 0$, a zero gradient Neumann pressure boundary condition is applied such that $(\partial p/\partial n = 0)$, and the VoF volume fraction is set constant such that $\alpha = 1$. The free surface elevation above still water level is given by

$$\gamma(0, t) = \frac{H}{2}\cos(\kappa x - \omega t) \tag{9}$$

where γ is the elevation from the SWL and κ is the wave number. A damping zone is located in front of the right hand, wave absorbing boundary, such that at $x = L, u(L, t) \to 0$ and $\gamma(L, t) \to 0$.

The wave tank uses a relaxation-based wave generation and absorption scheme. Using the symbol Ψ to generalize the formulae to include $\mathbf{u}$ and α respectively, the following relaxation equation, is used to ensure that the computational values of $\mathbf{u}$ and α (Ψ_cp) are consistent with the analytical values (Ψ_an) at the interface between relaxed and non-relaxed zones,

$$\Psi = \Phi\Psi_\mathrm{cp} + (1 - \Phi)\Psi_\mathrm{an}. \tag{10}$$

where the relaxation parameter for the generation zone of length L_{gen} is computed through,

$$\Phi_{\text{gen}} = 1 - \frac{\exp[(\frac{x}{L_{\text{gen}}})^{3.5}] - 1}{\exp[1] - 1}, \tag{11}$$

while that of the absorption zone of length L_{ab} according to

$$\Phi_{\text{ab}} = 1 - \frac{\exp[(1 + \frac{x-L}{L_{\text{ab}}})^{3.5}] - 1}{\exp[1] - 1}. \tag{12}$$

The free surface of the incident wave is described as $S(x, y, t) = z - \gamma(x, y, t) = 0$. The velocity at this boundary is set in accordance with the kinematic free surface boundary condition (KFSBC). For fluid particles adjacent to the free surface, a condition linking the velocity of the boundary to that of the particles is imposed as given by considering the two phases bridged by the surface, $S(x, y, t) = 0$, from which it follows that, either side of the boundary,

$$\frac{\partial S}{\partial t} + \mathbf{u} \cdot \nabla S = 0. \tag{13}$$

where ∇S is normal to the surface $S(x, y, t) = $ constant, implying the unit normal $\mathbf{n}$ is given by

$$\mathbf{n} = \frac{\nabla S}{|\nabla S|} = \frac{\partial \gamma / \partial t}{\sqrt{(\partial \gamma / \partial x)^2 + 1}}, \qquad y = \gamma(x, t). \tag{14}$$

Upon finding the difference between the two interface equations corresponding to either phase according to equation (13), the following condition holds true at the free surface

$$\mathbf{u}^{(\text{d})} \cdot \mathbf{n} = \mathbf{u}^{(\text{w})} \cdot \mathbf{n}, \qquad S(x, y, t) = 0. \tag{15}$$

The initial conditions are as follows. At $t = 0$,

$$u(x, 0) = U_{\text{m}} \quad \text{and} \quad \gamma(x, 0) = \frac{H}{2} \cos(\kappa x). \tag{16}$$

2.1. Numerical model

Numerical resolution of the air-water phases was accomplished by the use of OpenFOAM© libraries (see Jacobsen et al., 2012) which contain a wave generation and absorption toolbox.

Spatial discretisations of the pressure gradient, divergence and Laplacian terms of the mass conservation and Navier-Stokes equations are achieved via a standard Gaussian finite volume integration method. The resulting second-order scheme has fewer stability issues compared to more accurate but rather unstable higher-order schemes, especially in the context of gravity wave flows. Time integration is undertaken using a Crank-Nicolson scheme. Since an explicit expression for pressure does not exist owing to the coupling between the velocity and pressure terms in the incompressible Navier-Stokes equation,

application is necessary of the PISO (Pressure Implicit with Splitting of Operators) algorithm, that enables the use of the continuity and momentum equations to introduce a pressure expression in the form of a Poisson equation Combination of the momentum prediction and pressure correction steps associated with PISO, leads to the solution of the Navier-Stokes equation.

To satisfy the free surface pressure boundary condition, cells in close proximity to the free surface are identified either as dry cells (above the free surface) or wet cells (below the free surface). As seen from figure 2, two neighbouring cells, one dry and the other wet, either side of the free surface are used for interpolation purposes. Following solution of the Navier-Stokes equations for the pressure field, the total pressure (dynamic and hydrostatic) of the wet cell, p_{w} is obtained. By setting atmospheric pressure (which represents the pressure of the dry cell) to p_{o}, the free surface pressure boundary condition becomes:

$$p_{i,j} = [1 - \epsilon]p_{\mathrm{w}} + \epsilon p_{\mathrm{o}}, \tag{17}$$

where i, j represent the cell indices, $\epsilon = d_{\mathrm{wd}}/d_{\mathrm{w}}$ in which d_{wd} is the distance between the centres of the neighbouring cells either side of the free surface, and d_{w} is the distance between the centre of the wet cell and the free surface.

To ensure the bed is impermeable, a no-slip condition is applied at the bottom boundary, $\mathbf{u} = 0$, along with Neumann conditions for both the volume fraction and pressure. A Dirichlet condition $\mathbf{u} = 0$ is applied at the outlet, where the volume fraction and pressure boundaries again are represented by Neumann conditions.

To obtain a viable solution for FSI problems involving free surface waves, we must achieve seamless treatment of the interface between the fluid and the solid structure and an appropriate resolution of the free surface. The DFIB method eliminates need for an adaptive mesh; instead a fixed Cartesian mesh suffices. This property is particularly useful for cases involving moving bodies, which would otherwise require re-meshing at every time step. Mohd-Yusof (1997) was one of the first to propose DFIB, which was later applied to three-dimensional complex flows (Fadlun et al., 2000). Unlike previous formulations, which relied heavily on interpolation schemes, the present direct forcing method uses an indicator function η as the key identifier for the solid ($\eta = 1$) and fluid ($\eta = 0$) regions. An improved sub-grid setup is applied around the virtual solid boundary (figure 3), resulting in a distinct interface where, $0 < \eta < 1$. The DFIB method is executed by inclusion of the direct forcing function $\mathbf{f}$, on the RHS of equation (2). This function is derived and implemented as follows:

$$\mathbf{f}^{m+1} = \eta^{m+1}\left(\frac{\mathbf{u}_s^{m+1} - \mathbf{u}^{**}}{\Delta t}\right) \tag{18}$$

and

$$\mathbf{u}^{m+1} = \mathbf{u}^{**} + \mathbf{f}^{m+1}\Delta t \tag{19}$$

where $\mathbf{u}_s$ and $\mathbf{u}^{**}$ are the solid and solenoidal fluid velocity fields respectively. Clearly $\mathbf{f}^{m+1}$ mimics an additional momentum on the fluid owing to the solid motion. In regions remote from the solid/fluid interface, the indicator function η is determined by:

$$\eta(x, y, t) = \begin{cases} 1, & (x - x_c(t))^2 + (y - y_c(t))^2 \le R^2 \\ 0, & (x - x_c(t))^2 + (y - y_c(t))^2 > R^2 \end{cases} \tag{20}$$

where R is the radius of the cylinder, (x, y) are the coordinates of the centre of the grid cell under consideration, and (x_c, y_c) are the coordinates of the cylinder. Within the solid/fluid interface, a sub-grid approach that enables capture of a sharper boundary is deployed such that

$$\eta_{i,j} = \frac{\Sigma \xi_{k,l}}{N \times N} \tag{21}$$

where k, l are the updated cell indices upon the determination of $\xi_{k,l}$ in each sub-cell by equation (20).

The Volume of fluid method (Hirt and Nichols, 1981) is used to capture the free surface by means of an indicator function α, to distinguish the Newtonian air-water phases and also to enable determination of the density and viscosity of the respective phases. Within the interface $0 < \alpha < 1$, while elsewhere α is respectively 0 and 1 for the lighter and denser phases. Assuming both phases are incompressible, the transport equation (applicable solely at the interface) that describes the temporal evolution of the conservative variable α may be expressed by

$$\frac{\partial \alpha}{\partial t} + \nabla \cdot (\alpha \mathbf{u}) + \nabla \cdot (\alpha(1 - \alpha)\mathbf{u}_{\text{ac}}) = 0 \tag{22}$$

Note that the LHS includes an additional term based on the artificial compression velocity $\mathbf{u}_{\text{ac}}$. Equation (22) is integrated in time using a similar scheme to that for the Navier-Stokes equation. The divergence term is discretized according to the second-order accurate Gaussian MUSCL (Monotonic Upstream-Centered Scheme for Conservation Laws) scheme, formulated by van Leer (1979). The equation of motion of the cylinder (3) is integrated forward in time using Butchers 5th order Runge Kutta scheme.

We now briefly outline the numerical procedure used to implement the DFIB model for FSI such that the no-slip boundary condition at the cylinder-fluid interface is satisfied. The fluid velocity field is updated using the forcing function $\mathbf{f}^m$, given by equation (18).Commencing with values of $\mathbf{u}^m, p^m$ and $\mathbf{f}^m$ from the mth time step, the time marching procedure from the mth to the $m + 1^{th}$ time step is:

(1) Determine $\mathbf{u}_s^{m+1}$ and $\mathbf{x}_s^{m+1}$ by numerical differentiation of the ODE in equation (3).
(2) Update Ω_s^{m+1} and η^{m+1} according to Eqs.(20) and (21).
(3) Solve the Navier-Stokes equation (2) without $\mathbf{f}$ and pressure gradient.
(4) Implement the PISO algorithm.
(5) Determine $\mathbf{f}^{m+1}$ using equation (18).
(6) Update the fluid velocity $\mathbf{u}^{m+1}$, according to equation (19).
(7) Evaluate the resultant force on the cylinder by equation (4).
(8) Repeat steps 1 to 7 to advance to the $m + 1^{th}$ time step.

3. Results and discussion

We consider a numerical wave tank of 17.5 m length and still water depth 0.6 m. The (undisturbed) centre of the cylinder is initially located 0.35 m below still water level, halfway along the tank. The flow parameters are set such that the Reynolds Re = $U_mD/\nu = 110$, Keulegan-Carpenter number KC = $U_mT/D = 10$, and Froude number Fr = $U_m/\sqrt{gD} = 0.69$, in which ν is the fluid kinematic viscosity, D the cylinder diameter, and T the wave period. The Ursell number, $U_{rs} = H\lambda^2/d^3 \approx 12$ (where H is wave height, λ is the wave length, and d is the water depth), is much less than 100, and so corresponds to small amplitude waves such that linear wave theory applies. The hydroelastic behaviour of the cylinder is partly characterized by the reduced velocity $U_R^* = U_m/f_nD$ where f_n is the natural frequency of the cylinder in water. A range of reduced velocities $4 < U_R^* < 10$ is considered in the parameter study. The variation of U_R^* is implemented by altering U_m. By adjusting T from a value of 10 s for $U_R^* = 5$ to the appropriate values for the other reduced velocities, the KC number is kept constant. The remaining structural non-dimensional mass and damping parameters are set to $m_s^* = m_s/\rho\pi D^2 = 3.17$ and $m_s^*\zeta = 0.01$ (where ζ is the damping ratio). Table 1 summarizes the structural characteristics of the horizontal cylinder as a SDOF system. Table 2 lists the incident wave conditions considered in the parameter study.

Figure 4 shows the non-uniform computational mesh which has a prescribed limiting cell aspect ratio, and is based on a Cartesian framework. To satisfy the cell aspect ratio, a geometric progression function is applied to create the non-uniform mesh. The ratio between the size of the cells in the region immediately surrounding the cylinder to those at the extreme ends of the NWT is 0.025. The number of cells within the refined region close to the cylinder is 70 x 70. The non-uniform cell regions consist of 200 cells horizontally and 150 cells vertically, either side of the cylinder. A time step of 10^{-3} s is used. The convergence criterion is based on the solution of the pressure equation and is set at 1×10^{-4}. Considering the case of $U_R^* = 5$, the overall mean Courant number realised is ≈ 0.00035 and the maximum Courant number ≈ 0.035. All computations were undertaken on an Intel® Xeon CPU E31275 operating at 3.40GHz. Complete domain results were recorded every 0.05 s. Parallel programming using four cluster nodes and based on MPIRUN led to an execution time of 130 hours and a runtime of 800 to 1000 s per case.

3.1. Model validation tests

We first describe results from grid independence tests. Figure 5 shows the time history of the motion of the centre of the cylinder from $t = 62$ s to $t = 93$ s for $U_R^* = 4.8$ on three grids; fine, with $\Delta x = \Delta y = 0.0256D$; medium, with $\Delta x = \Delta y = 0.0286D$; and coarse, with $\Delta x = \Delta y = 0.0313D$. Close agreement is achieved between the results on the medium and fine grids, showing the evolution of flow-induced vibration of the cylinder as it begins to saturate with a transverse excursion amplitude of about 0.02 m. For the tests discussed below we select the medium grid as being suitable.

Previous validation of the DFIB model includes the study by Noor et al. (2009) who simulated unidirectional flow past a stationary circular cylinder. Noor et al. obtained a mean drag coefficient and wake length for Re = 40 and a drag coefficient and Strouhal number for Re = 100 that compared satisfactorily with alternative numerical results presented by Su et al. (2007). Noor et al. also obtained drag coefficients and Strouhal numbers for two cylinders in tandem and interacting with uniform fluid flow at Re = 200 in close agreement with results obtained by Meneghini et al. (2001).

Chern et al. (2012) used the present DFIB model to predict the benchmark case of oscillatory flow past a stationary cylinder at Re = 200 and KC = 10 and determined the hydrodynamic loading on an array of cylinders in agreement with data by Iliadis and Anagnostopoulos (1998). Further validation concerning the evolution of the wake of a single circular cylinder in oscillatory flow is described by Chern et al. (2013), whose results were again similar to those obtained by Iliadis and Anagnostopoulos (1998). These studies demonstrate that the DFIB model provides accurate representation of uniform and oscillatory flow for FSI cases at low Reynolds numbers (i.e. in the fully laminar flow regime).

We now consider verification of the model based on DFIB coupled with VoF methods by first simulating a fixed then a moving horizontal cylinder submerged in a progressive wave train. Figures 6 a and b display the validation of the horizontal and vertical components of the velocity profiles for three cross sections ($x^* = x/D$ = -0.6, $x^* = 0$ and $x^* = 0.6$), at phase time $t = nT + T/2$, for the fixed cylinder case (Re = 100 and KC = 5). The experimental and numerical data used for comparison are taken from the work of Dutsch et al. (1998). The velocity profiles compare well with the given data except for a few points above $y^* = y/D = 0$, especially for the u^* profile at $x^* =$ -0.6. This anomaly is likely due to the fact that the setup of Dutsch et al. (1998) was without a free surface, whilst the present case has a free surface. This fact introduces the effect of ellipticity on the behaviour of the velocity profiles. For the moving cylinder case (Re = 110 and KC = 10) a plot of non-dimensional frequency $f_n^* = U_R^* f_w^*/KC$ (where $f_w^* = f/f_w$) against reduced velocity U_R^* is shown in figure 7. In this figure the present model predictions and an analytical solution derived by Sumer and Fredsøe (1988) are superimposed. The agreement is excellent either side of the lock-in regime, for $4.5 < U_R^* < 4.67$ and $4.93 < U_R^* < 5.2$, with the present model also capturing the lock-in behaviour in the region $4.7 < U_R^* < 4.9$, where the vortex shedding frequency shifts to the natural frequency of the structure. Two other features are worth mentioning. Given that that wave motion is somewhat akin to oscillatory flow, a previously shed vortex returning towards the cylinder when the flow reverses may hit the cylinder, leading to a frequency response slightly above that of the analytical solution at, say for example $U_R^* = 4.63$. Additionally, wave flow (unlike steady current and planar oscillatory flow) is composed of particles in orbital motion. Vortices in the proximity of the cylinder are influenced by this orbital motion, thus delaying detachment leading to a frequency response slightly below that of the analytical solution at, say for example $U_R^* = 5.1$.

3.2. Parameter study

The DFIB-VoF model is now used to investigate wave-cylinder responses in the laminar flow regime over a range of reduced velocities, $4 < U_R^* < 10$. Animation videos of selected velocity and vorticity field results are available in $anim1\_10ReversibleFlowVect.avi$ and $anim1\_10ReversibleFlowVort.avi$. These vector and vorticity patterns have been extracted for the case of lock-in reduced velocity $U_R^* =$4.8 during one wave half cycle.

Figures 8 and 9 show the flow velocity vector and vorticity fields in the vicinity of the responding horizontal cylinder under progressive waves at lock-in during part of a vortex-shedding cycle, where KC = 10 and $U_R^* =$4.8. The upper insert in figure 8 shows the free surface time history of the wave, indicating at what points in the cycle the results have been extracted. Figure 8(a) and figure 9(a) illustrate the flow pattern at $t = 164.75$ s, when the cylinder is located almost exactly at its mean position, and the wave free surface above the cylinder is approaching a trough. The wave flow is predominantly from right to left. This flow impacts on the right hand side of the cylinder, helping to drive the shear layers coming off the top and bottom of the cylinder, which are rolling up into a pronounced clock-wise rotating vortex behind the cylinder along with the early stages of an anticlockwise dominated flow immediately above the cylinder. Two previously shed vortices can be seen above (clockwise) and below (anticlockwise). Earlier vortices can also be discerned leftward (above) and to the right of the domain. The motion of the cylinder with respect to the fluid means that the developing shear layers are on one side displaced slightly downwards away from the lower surface of the cylinder and on the other side squeezed against the upper surface. Figure 8(b) and figure 9(b) correspond to the arrival of the wave trough directly above the cylinder at $t = 165.35$ s, accompanied by growth of the free shear layers and the cylinder having commenced its downward response motion under the influence of the attached clockwise vortex. The wake region also begins to develop. By $t = 166.45$ s (figures 8(c) and 9(c)) the flow field resembles more closely a unidirectional flow pattern, with a pronounced wake region (the clockwise vortex having shed), and the anticlockwise vortex strengthening ready to shed behind the cylinder. This is characteristic of lock-in. Upper and lower wall boundary layers are clearly evident. Residual vorticity previously below the cylinder has been convected far to the left, and the clockwise vortex originally above the cylinder is beginning to dissipate having also moved leftwards due to convection in the wave flow field. This flow pattern corresponds to the largest transverse displacement response of the cylinder, even though the wave trough has just passed. By $t = 167.35$ s, as shown in figures 8(d) and 9(d), the cylinder has returned to its mean position, and the wave surface is nearing mean water level. Overall the velocity field has weakened, as the x-direction flow component is beginning to change direction to flow from left to right. The core positions of the shed clockwise and developing anticlockwise vortices in the residual wake remain fairly static, nevertheless resembling a Kármán vortex street, although the cylinder has moved upwards (pushing against the upper shear layer) and the anticlockwise attached vortex has slightly elongated. Figures 8(e) and 9(e) illustrate the situation at $t = 169$ s, when

the wave-driven flow is now predominantly from left to right (as the crest is about to arrive). The anticlockwise vorticity immediately above the cylinder is disrupted by the development of a new clockwise shear layer penetrating eastwards along the upper surface of the cylinder. The strong anticlockwise vortex that was previously in the wake immediately to the left of the cylinder begins to migrate below the cylinder feeding on vorticity added from the lower boundary layer, and strengthens as it passes below (as can be seen shortly afterwards in figure 8(f) at $t = 170$ s, which corresponds almost to the wave crest being located above the cylinder). Other residual vortices surround the cylinder. At $t = 170$ s, a previously shed anticlockwise vortex is convected eastwards impacting against the cylinder, and forcing it downwards. By this stage, it can be seen that the cylinder is situated in a soup of vortices (growing and residual), and developing boundary layers. This behaviour is consistent with the findings of Borthwick (1986) on orbital flow past a cylinder. It should also be noted that the vector and singly-paired vortex shedding patterns observed in figures 8 and 9, are similar to those observed by Williamson (1985), for similar Re and KC numbers.

Figure 10 depicts the dependence of the root-mean-square inline and transverse force coefficients, C_{frms} and C_{lrms}, on reduced velocity. The striking effect of lock-on is evident by the peaks in both coefficients in the range $4.7 < U_R^* < 4.9$, where C_{frms} reaches 1.8 and C_{lrms} reaches 1.5. Both coefficients have lower more constant values of $C_{frms} \approx 1.5$ and $C_{lrms} \approx 0.5$ for $4.5 < U_R^* < 4.67$ and $C_{frms} \approx 1.5$ and $C_{lrms} \approx 0.4$ to 0.7 for $4.93 < U_R^* < 5.2$. Figure 11 displays spectra obtained from the inline and transverse force coefficient time series against the frequency ratio ($f_w^* = f/f_w$) for different values of U_R^*. Here f refers to the frequency of the force time series. For $4.3 < U_R^* < 4.8$, peaks occur at $f_w^* = 1$ for the inline force component and for the transverse (lift) force component, the latter in agreement with experimental observations by Williamson (1985). For the upper range of reduced velocities $5 < U_R^* < 10$, the frequencies of both the inline and transverse force components become synchronized with the wave frequency, though it should be noted that the amplitudes of these components are very small compared to their counterparts in the lower and lock-in regimes. Figure 11 also shows that the transverse force spectral component is very much smaller than that of the inline force, except for lock-in when the spectral peak corresponding to the lift force coefficient is of similar magnitude to that of the inline force coefficient.

Figures 12, 13 and 14 present time histories and associated frequency spectra of the transverse displacement response of the cylinder for cases corresponding to the three different flow regimes. Figure 12 shows the results obtained for the lower beating mode ($4.3 < U_R^* < 4.5$), where it can be seen that the cylinder vibrates in bursts of activity at frequency ratios $f_n^* = f/f_n$ of between 0.8 and 0.9. Here f refers to the frequency of displacement vibration. Figure 13 shows the corresponding results for the lock-in mode. Here the cylinder vibrates at frequencies that are quite close to the natural frequency ($0.95 < f_n^* < 0.98$). The upper beating mode has a wider range of reduced velocities as shown in figure 14. For $U_R^* = 5$ and 10, the non-dimensional beating frequency is exactly 1. This mode can also be discerned in other cases, especially at $U_R^* = 8$, where

the vibration frequency is much less than the natural frequency ($f_n^* = 0.8$). Overall the amplitude of transverse vibration within the lock-in range ($4.7 < U_R^* < 4.9$) is the largest of all the vibration modes, where it becomes highly repeatable as the flow-induced displacements reach saturation. Considering figures 12, 13 and 14, and given that f_w^* increases with increasing U_R^*, it can be easily shown that the lower beating and lock-in modes have peaks at a common vibration to wave frequency ratio $f_w^* = 2$. Similarly it can be shown that for the upper beating mode, $f_w^* = 1$, with the exception of $U_R^* = 10$ which records a vibration to wave frequency ratio f_w^* of 2.

Figure 15 shows the dependence of the non-dimensional amplitude response (normalized by the cylinder diameter, such that $A^* = A/D$) on reduced velocities. The amplitude response peaks within the lock-in range. In this case, the reduced velocity range for the lock-in regime is quite narrow, unlike the corresponding case of a hydroelastically mounted cylinder in a unidirectional flow.

4. Conclusions

A numerical model was described that facilitates accurate predictions of the response behaviour of a flexibly mounted horizontal cylinder under progressive waves. The model utilized a combination of direct forcing boundary simulation and the volume of fluid method to represent the moving body and water free surface. The cylinder was represented as a single degree of freedom system in the vertical plane aligned with the direction of the waves. Mesh independence tests were used to assess satisfactory grid fineness and the time step was selected to ensure stability. Whereas validation studies concerning the present model (without VoF) have already been previously reported (Noor et al. 2009, Chern et al. 2012, 2013) for unidirectional and planar oscillatory flow past a stationary circular cylinder, the present paper describes satisfactory verification against Sumer and Fredsøe (1988) analytical solution of non-dimensional response frequency against reduced velocity for a horizontal fixed cylinder submerged in a progressive wave train.

A parameter study was conducted for a flexibly mounted horizontal cylinder in waves by varying the reduced velocity in the range $4 < U_R^* < 10$, while setting KC = 10, Re =110, and Fr = 0.69. It is found that the cylinder motions are strongly influenced by the local vorticity field supplied by vorticity injected into the flow as it separates at the cylinder surface, creating layers of high shear, which roll up into vortices that either squash against the surface as they rotate or detach and are swept around the cylinder due to the inherently orbital flow under the free surface waves. The cylinder is mounted in relatively shallow water so that both the effects of the free surface and the solid bed contribute to the local flow dynamics. The transverse force on the responding cylinder therefore contained contributions from the vertical structures in the flow field (as they reverse across the cylinder or rotate around it), the orbital wave field, and the proximity to the bed boundary. Three amplitude response regimes were identified: lower beating; lock-in; and upper beating modes. The lower beating mode was associated with a regular

but varying amplitude response. In the lock-in range, $4.7 < U_R^* < 4.9$, the vibration frequency remained close to the cylinders natural frequency, with the cylinder transverse displacement vibrations exhibiting large-amplitude repeatable oscillations. When in the upper beating mode, the frequency of cylinder vibrations became irregular. This latter result may be due to numerical limitations, and further computational research is needed to develop a more robust wave tank aimed at reproducing cylinder responses at higher reduced velocities. The current work has not established the reason for the amplitude modulation outside the lock-in range and this phenomenon should perhaps be given more attention in future. Although the model is limited to low Reynolds numbers corresponding to laminar flows and to two dimensions, its extension to turbulence modelling and three-dimensions should be straightforward.

Acknowledgements

References

Armenio V 1998 Dynamic loads on submerged bodies in a viscous numerical wave tank at small KC numbers *Ocean Eng.* **25**(10), 881–905.

Beji S and Battjes J A 1993 Experimental investigation of wave propagation over a bar *Coast. Eng.* **19**, 151–162.

Borthwick A G L 1986 Orbital flow past a cylinder: a numerical approach *Int. J. Numer. Meth. Fl.* **6**, 677–713.

Borthwick A G L and Herbert, D. M 1990 Resonant and non-resonant behavior of a flexibly mounted cylinder in waves *J. Fluid Struct.* **4**, 495–518.

Canan B and Serpil K 2014 Free surface wave interaction with an oscillating cylinder *Appl. Math. Letters* **27**, 79–84.

Chakrabarti S and Cotter D 1978 Analysis of a tower-tanker system *Proc., 10th Annu. Offshore Techn. Conf.* pp. 1301–1310.

Chern M J, Hsu W C and Horng T L 2012 Numerical prediction of hydrodynamic loading on circular cylinder array in oscillatory flow using direct-forcing immersed boundary method *J. Appl. Math.* **2012**.

Chern M J, Shiu W C and Horng T L 2013 Immersed boundary modeling for interaction of oscillatory flow with cylinder array under effects of flow direction and cylinder arrangement *J. Fluid Struct.* **43**, 325–346.

Choi D Y, Wu C H and Young C C 2010 An efficient curvilinear non-hydrostatic model for simulating surface water waves *Int. J. Numer. Meth. Fl.* **66**, 1093–1115.

Dean R G and Dalrymple R A 1984 *Water Wave Mechanics for Engineers and Scientists* 1st edn Prentice-Hall Int., Inc., London.

Dutsch H, Durst F, Becker S and Lienhart H 1998 Low-Reynolds-number flow around an oscillating circular cylinder at low keulegan-carpenter numbers *J. Fluid Mech.* **360**, 249–271.

Evans D V, Jeffrey D C, Salter S H and Taylor J R 1979 Submerged cylinder wave energy device: theory and experiment *Appl. Ocean Res.* **1**(1), 3–12.

Fadlun E A, Verzicco R, Orlandi P and Mohd-Yusof J 2000 Combined immersed-boundary methods for three dimensional complex flow simulations *J. Comput. Phys.* **161**, 35–60.

Han Y, Zhan J M, Su W, Li Y S and Zhou Q 2015 Comparison of flow fields induced by fixed and oscillatory vertical cylinders in regular waves using 3d numerical model *Ocean Eng.* **106**, 238–251.

Hideaki M and Young-Gill L 1990 Vortex motions about a horizontal cylinder in waves *Ocean Eng.* **17**(3), 279–305.

Hirt C W and Nichols B D 1981 Volume of fluid (VOF) method for the dynamics of free boundaries *J. Comput. Phys.* **39(1)**, 201–225.

Iliadis G and Anagnostopoulos P 1998 Viscous oscillatory flow around a circular cylinder at low Keulegan-Carpenter numbers and frequency parameters *Int. J. Numer. Meth. Fl.* **26**(4), 403–442.

Jacobsen N G, Fuhrman D R and Fredsøe J 2012 A Wave Generation Toolbox for the Open-Source CFD Library: OpenFOAM® *Int. J. Numer. Meth. Fl.* **70**(9), 1073–1088.

Kaye D and Maull D J 1993 The response of a vertical cylinder in waves *J. Fluid Struct.* **7**, 867–896.

Koji O and Yoshiho I 1996 Estimation of inertia forces on a horizontal circular cylinder in regular and irregular waves at low Keulegan-Carpenter numbers *Appl. Ocean Res.* **18**, 145–156.

Longoria R G, Beaman J J and Miksad R W 1991 An experimental investigation of forces induced on cylinders by random oscillatory flow *J. Offshore Mech. Arct.* **113**, 275–285.

Meneghini J R, Saltara F, Siqueira C L R and Ferrari J 2001 Numerical simulation of flow in interference between two circular cylinders in tandem and side-by-side arrangements *J. Fluid Struct.* **15**, 327–350.

Mohd-Yusof J 1997 Combined immersed-boundary/b-spline methods for simulations of flow in complex geometries *CTR Annu. Res.h Briefs, NASA Ames Res. Center for Turb. Res., Stanford, CA.* .

Morison J R, OBrien M P, Johnson J W and Schaaf S A 1950 The forces exerted by surface waves on piles *Petr. Trans.* **189**, 149–156.

Mouazé D and Bélorgey M 2003 Flow visualisation around a horizontal cylinder near a plane wall and subject to waves *Appl. Ocean Res.* **25**, 195–211.

Noor D Z, Chern M J and Horng T L 2009 An immersed boundary method to solve fluid-solid interaction *Comput. Mech.* **44**, 447–453.

Oshkai P and Rockwell D 1999 Free surface wave interaction with a horizontal cylinder *J. Fluid Struct.* **13**, 935–954.

Park Y S, Chen Z S and Kim W J 2010 CFD application to the evaluation of wave and current loads on cylindrical platform model for ocean wind turbine *Proc. 9th ISOPE Pacific/Asia Offshore Mech. Symp. Busan, Korea, November 14-17* .

Sarpkaya T 1976 In-line and transverse forces on smooth and sand-roughened cylinders in oscillatory flow at high Reynolds numbers *Nav. Postgrad. Sch. Tech. Report No. NPS-69SL76062, Monterey, CA, USA* .

Sawamoto M and Kikuchi K 1979 Lift force on a circular cylinder in plane oscillatory flow *Proc. Coast. Eng. JSCE (in Japanese)* **26**, 429–433.

Shen L and Chan E S 2008 Numerical simulation of fluid structure interaction using a combined volume of fluid and immersed boundary method *Ocean Eng.* **35**(9), 939–952.

Su S W, Lai M and Lin C A 2007 An immersed boundary technique for simulating complex flows with rigid boundary *Comput. Fluids* **36**, 313–324.

Sumer B and Fredsøe J 1988 Transverse vibrations of an elastically mounted cylinder exposed to an oscillating flow *J. Offshore Mech. Arct.* **110**, 387–394.

van Leer B 1979 Towards the ultimate conservative difference scheme, v. a second order sequel to godunov's method *J. Comput. Phys.* **32**, 101–136.

Williamson C H K 1985 Sinusoidal flow relative to circular cylinders *J. Fluid Mech.* **155**, 141–174.

Yang Y and Rockwell D 2004 Interaction of a deep-water wave with a vertical cylinder: flow structure and loading *J. Fluid Mech.* **520**, 267–295.

Tables and table captions

Table 1: Structural characteristics of the elastically mounted horizontal cylinder.

D (m)	k (N/m)	m_s (kg)	c (Ns/m)	$m_s{}^*$
0.035	0.02515	0.0159	0.00014	3.17

Table 2: Incident wave conditions considered in parameter study, for KC = 10.

U_R^*	H (m)	κ (rad/m)	f_w (Hz)	d (m)
4.3	0.0148	0.2235	0.0860	0.6
4.4	0.0152	0.2287	0.0880	0.6
4.5	0.0155	0.2340	0.0900	0.6
4.73	0.0164	0.2459	0.0946	0.6
4.77	0.0165	0.2480	0.0954	0.6
4.8	0.0166	0.2495	0.0960	0.6
5	0.0173	0.2600	0.1000	0.6
7	0.0242	0.3655	0.1400	0.6
10	0.0346	0.5264	0.2000	0.6
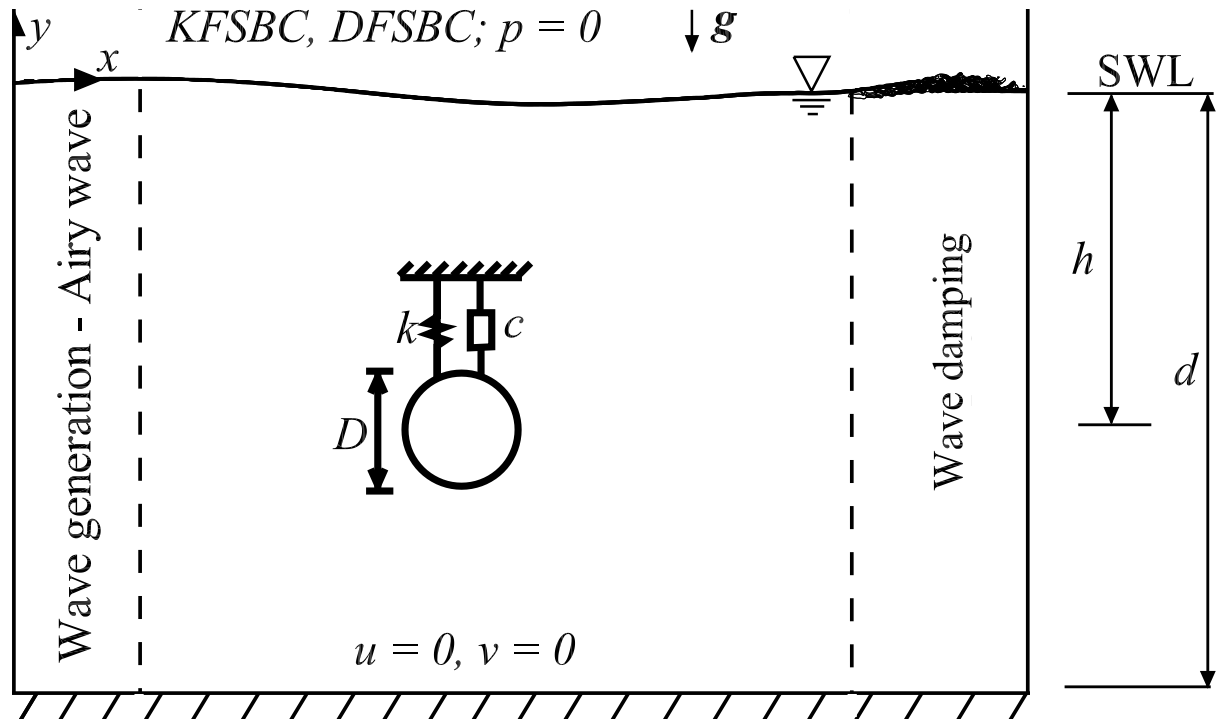
Figure 1: Numerical Wave Tank domain indicating wave generation and damping boundary zones, and key initial parameters.
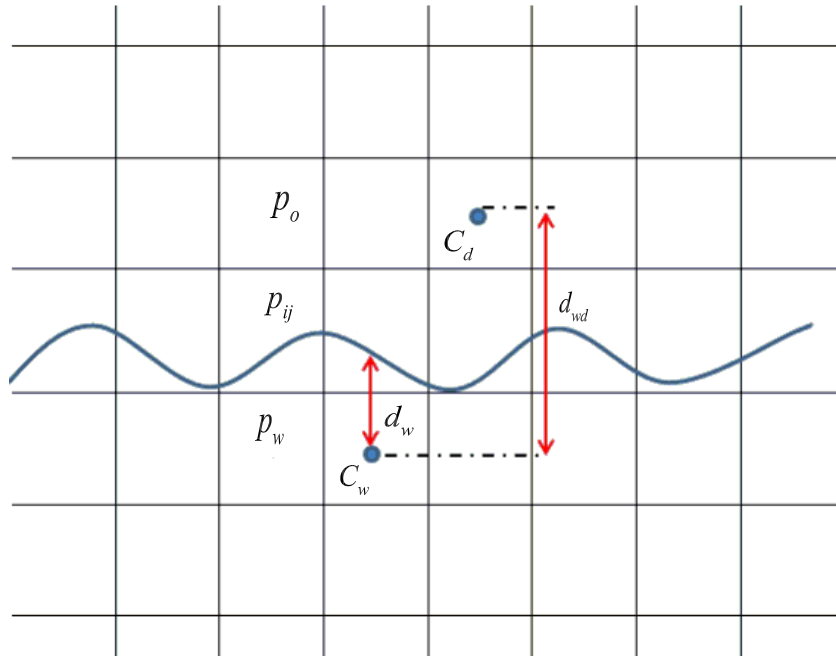
Figure 2: Numerical treatment of the pressure field close to the free surface.
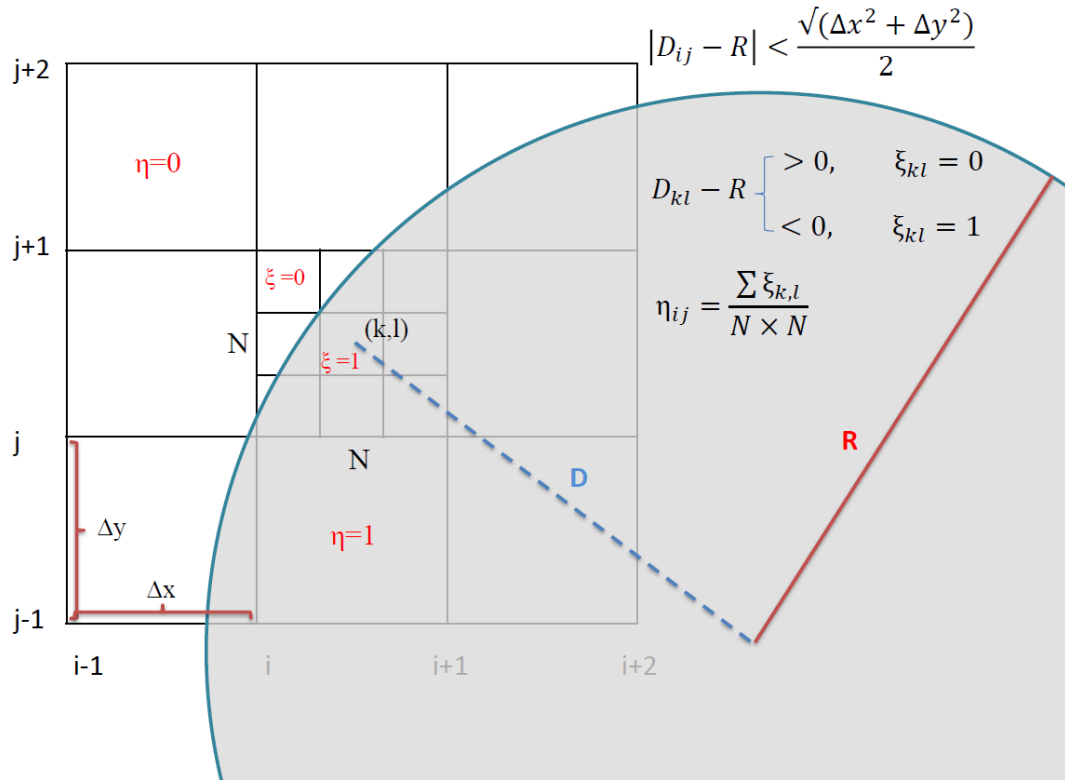
Figure 3: Illustration of direct forcing immersed boundary.
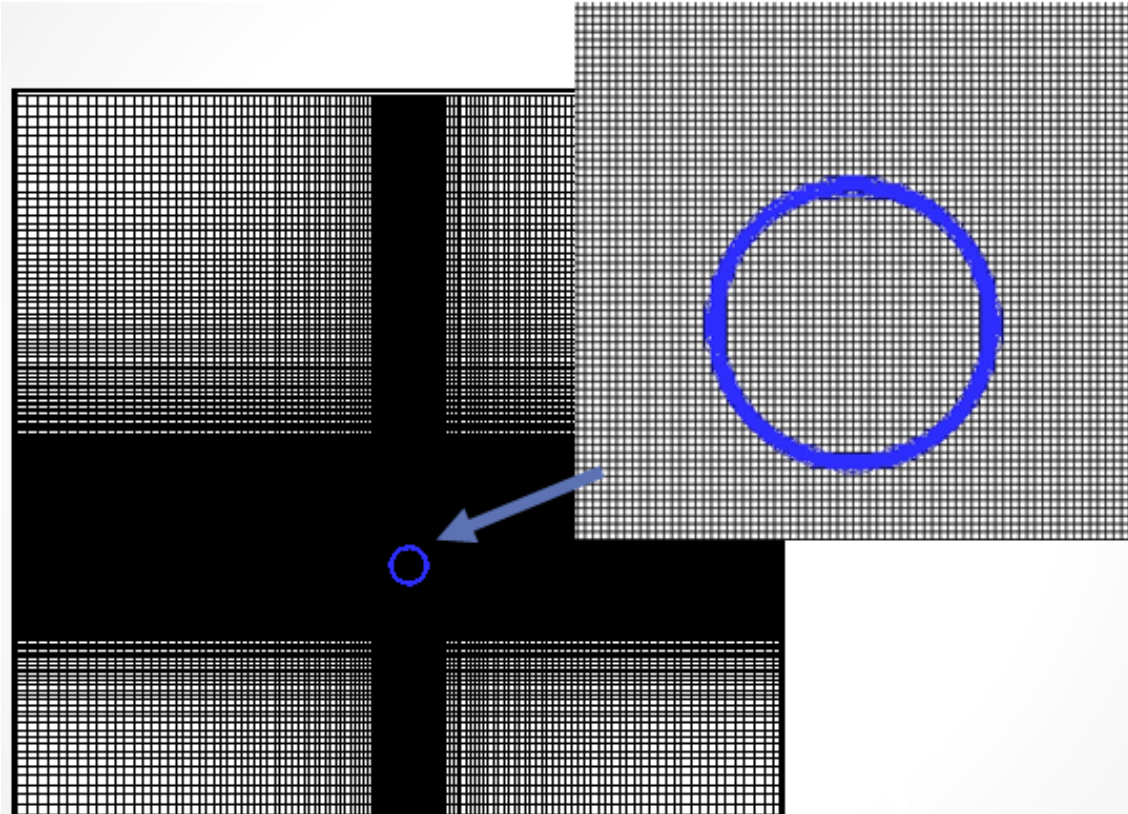
Figure 4: Computational mesh.
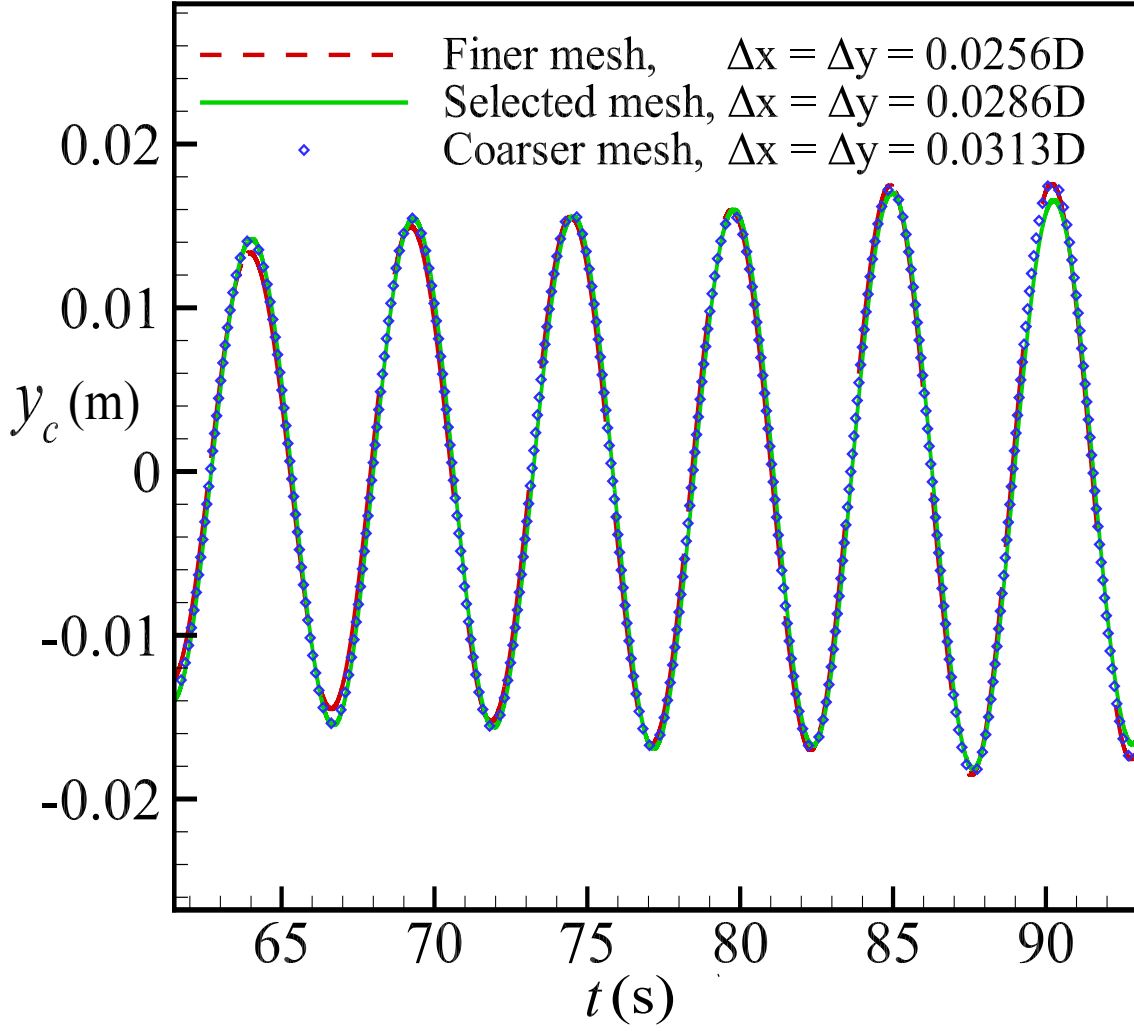
Figure 5: Grid independence test: time history of cylinder transverse motions for KC = 10, $U_R^* = 4.8$, $m^*\zeta = 0.01$.
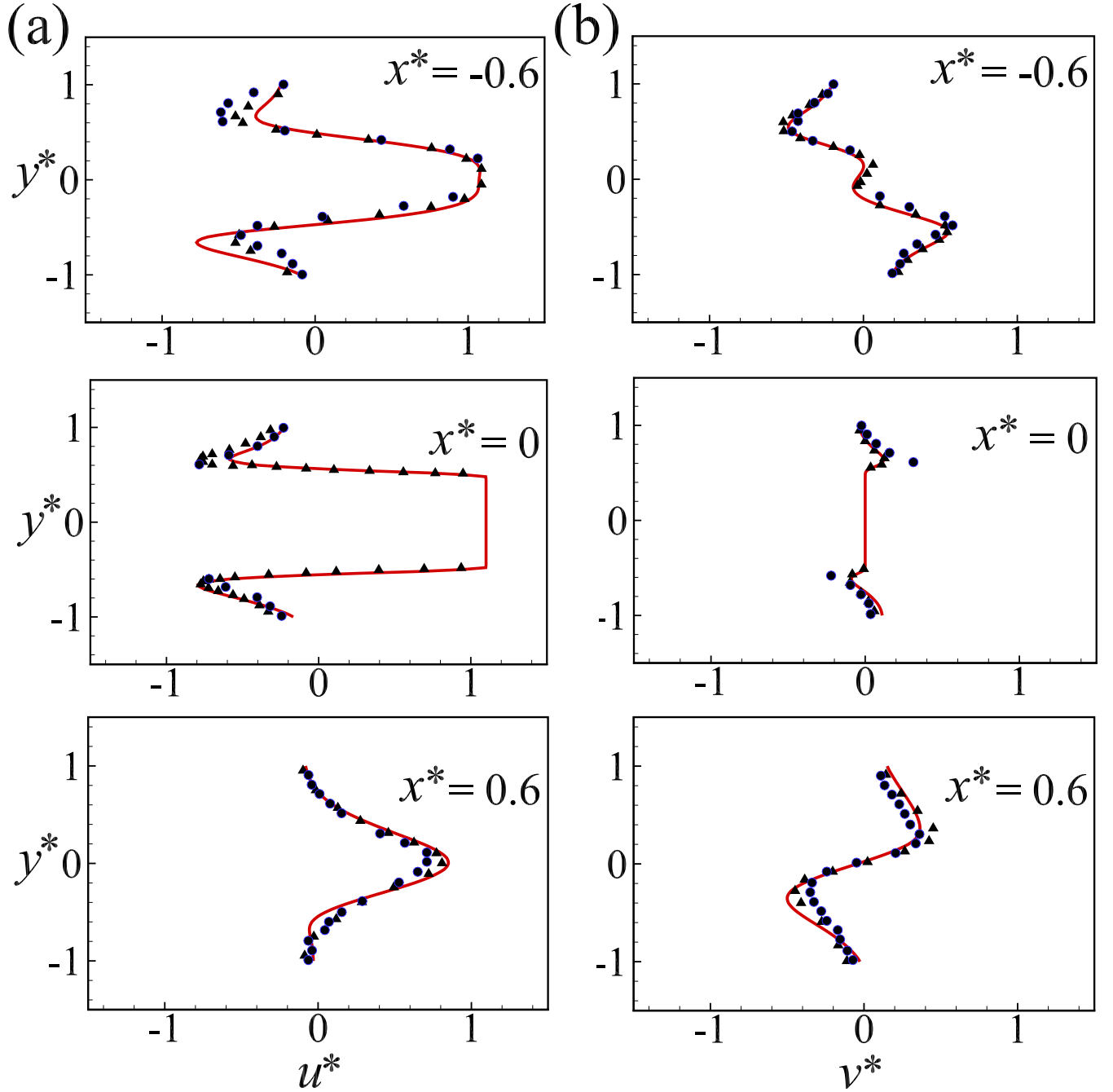
Figure 6: Comparing profiles for the non-dimensional velocity components (a) $u^* = u/U_{\mathrm{m}}$ (b) $v^* = v/U_{\mathrm{m}}$ for three cross sections ($x^* = $ -0.6, $x^* = 0$ and $x^* = 0.6$) at time $t = nT + T/2$, along $y*$. ●Experiment (Dutsch et al., 1998); ▲ numerical data (Dutsch et al., 1998); ——present numerical data.
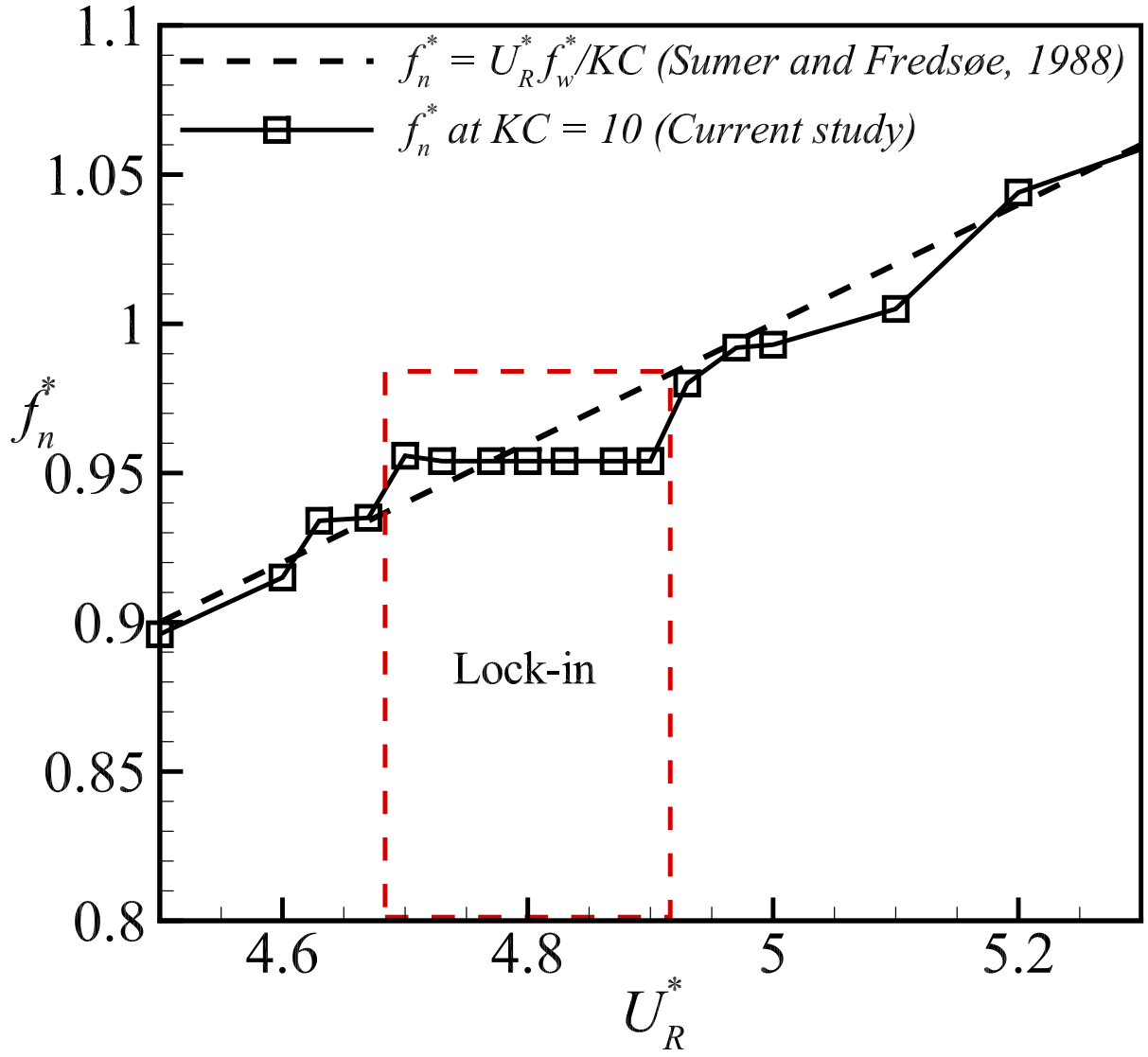
Figure 7: Variation in non-dimensional frequency $f_n^* = U_R^* f_w^*/KC$ (where $f_w^* = f/f_w$) with reduced velocity U_R^*, at KC = 10, $m^*\zeta = 0.01$, comparing present model predictions against the analytical solution derived by Sumer and Fredsøe (1988).
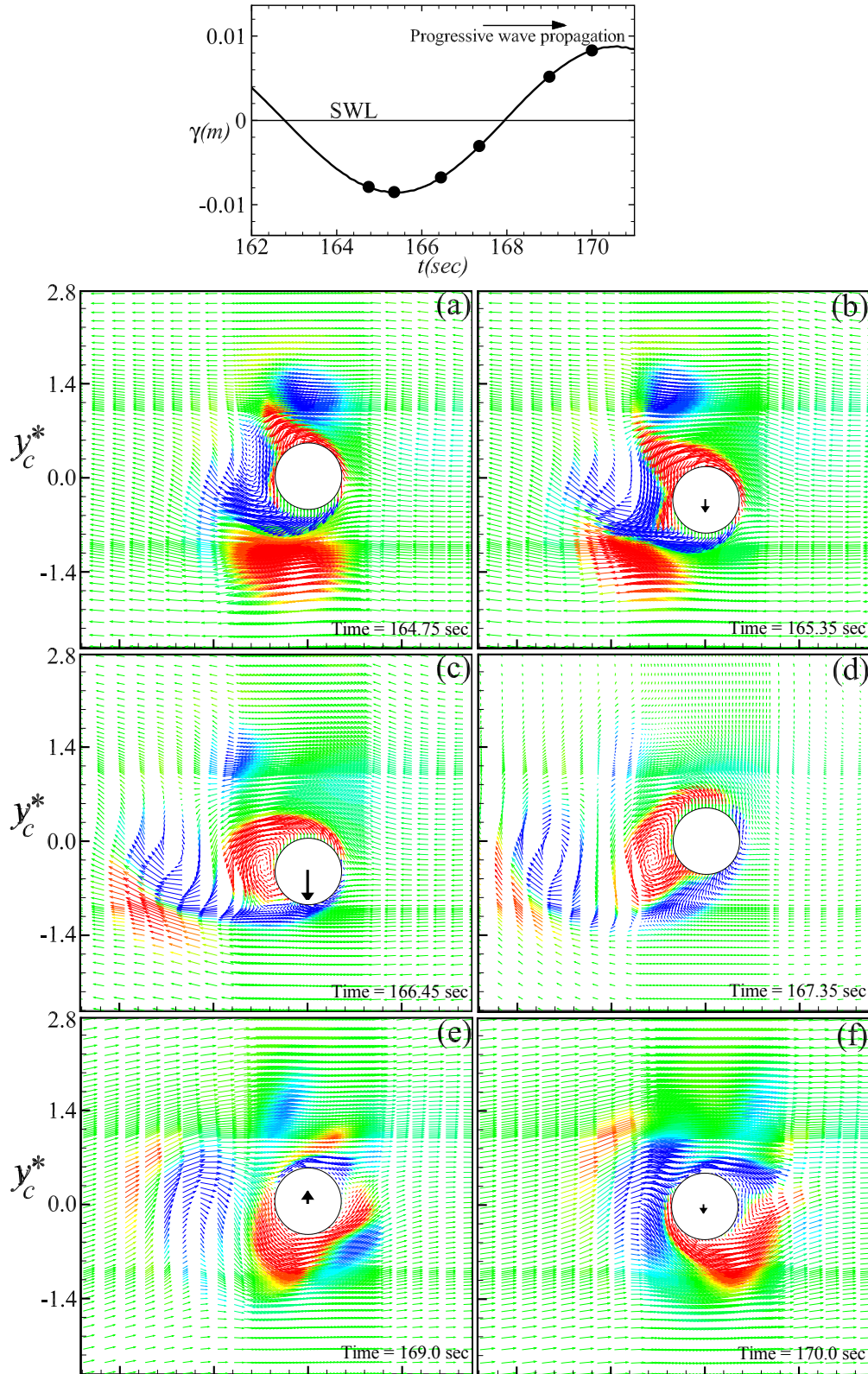
Figure 8: Flow velocity vector fields in the vicinity of a responding horizontal cylinder under regular waves at lock-in during part of a vortex-shedding cycle, for KC = 10 and $U_R^* = 4.8$: (a) $t = 164.75$ s; (b) $t = 165.35$ s; (c) $t = 166.45$ s; (d) $t = 167.35$ s; (e) $t = 169.0$ s; and (f) $t = 170.0$ s. Red vectors correspond to anticlockwise vorticity; blue vectors correspond to clockwise vorticity; and green vectors to negligible vorticity.
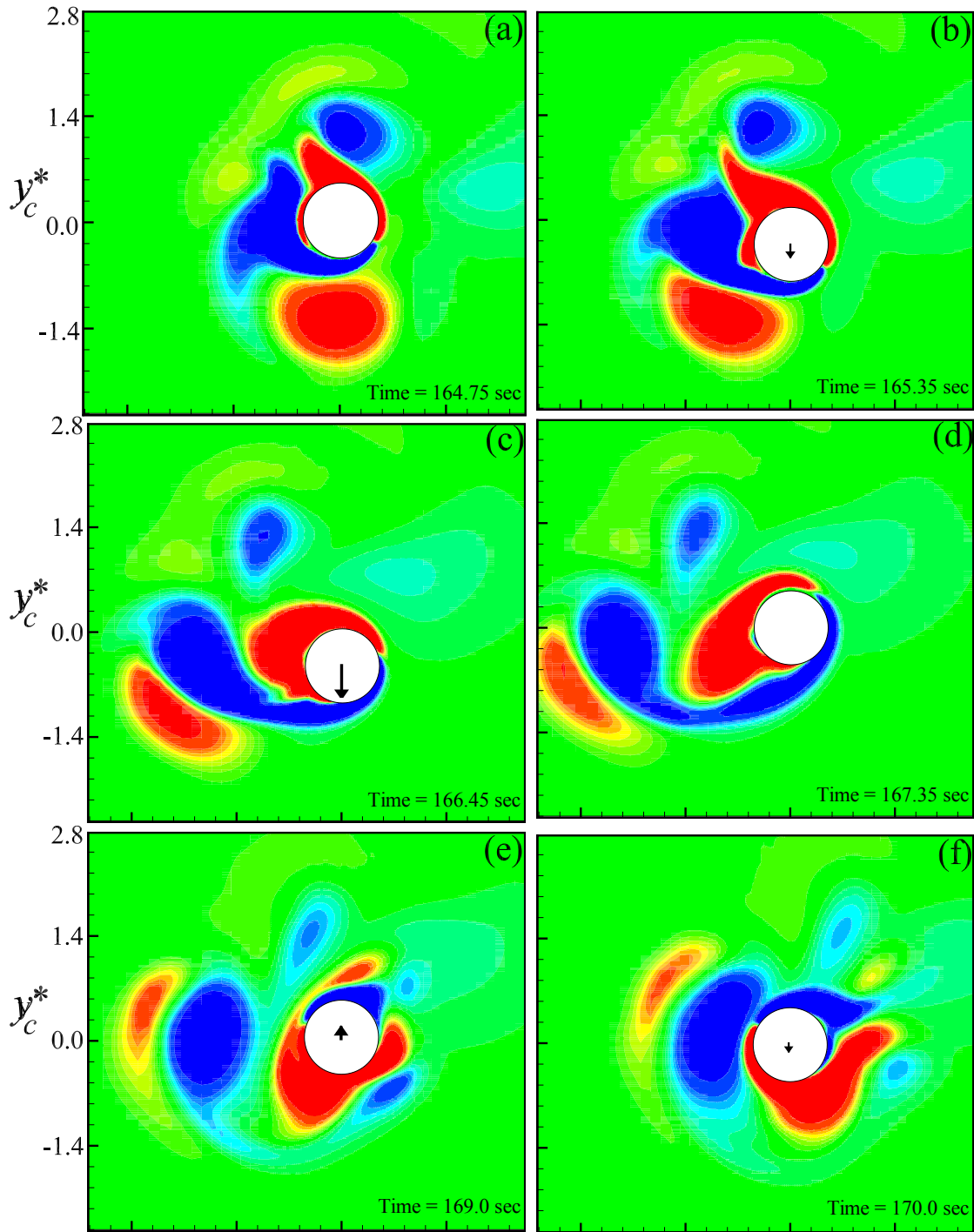
Figure 9: Vorticity patterns in the vicinity of a responding horizontal cylinder under regular waves at lock-in during part of a vortex-shedding cycle, for KC = 10 and $U_R^* = 4.8$: (a) $t = 164.75$ s; (b) $t = 165.35$ s; (c) $t = 166.45$ s; (d) $t = 167.35$ s; (e) $t = 169.0$ s; and (f) $t = 170.0$ s. Anticlockwise vorticity is denoted red; clockwise blue.
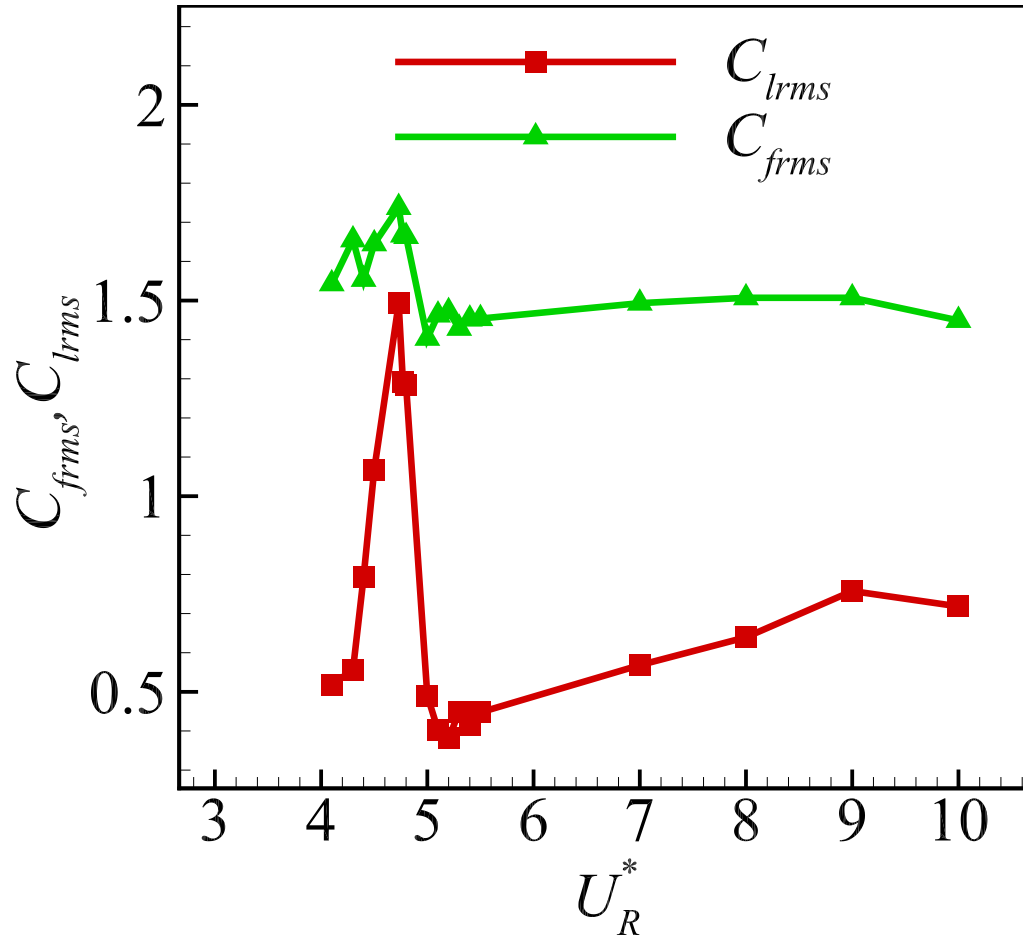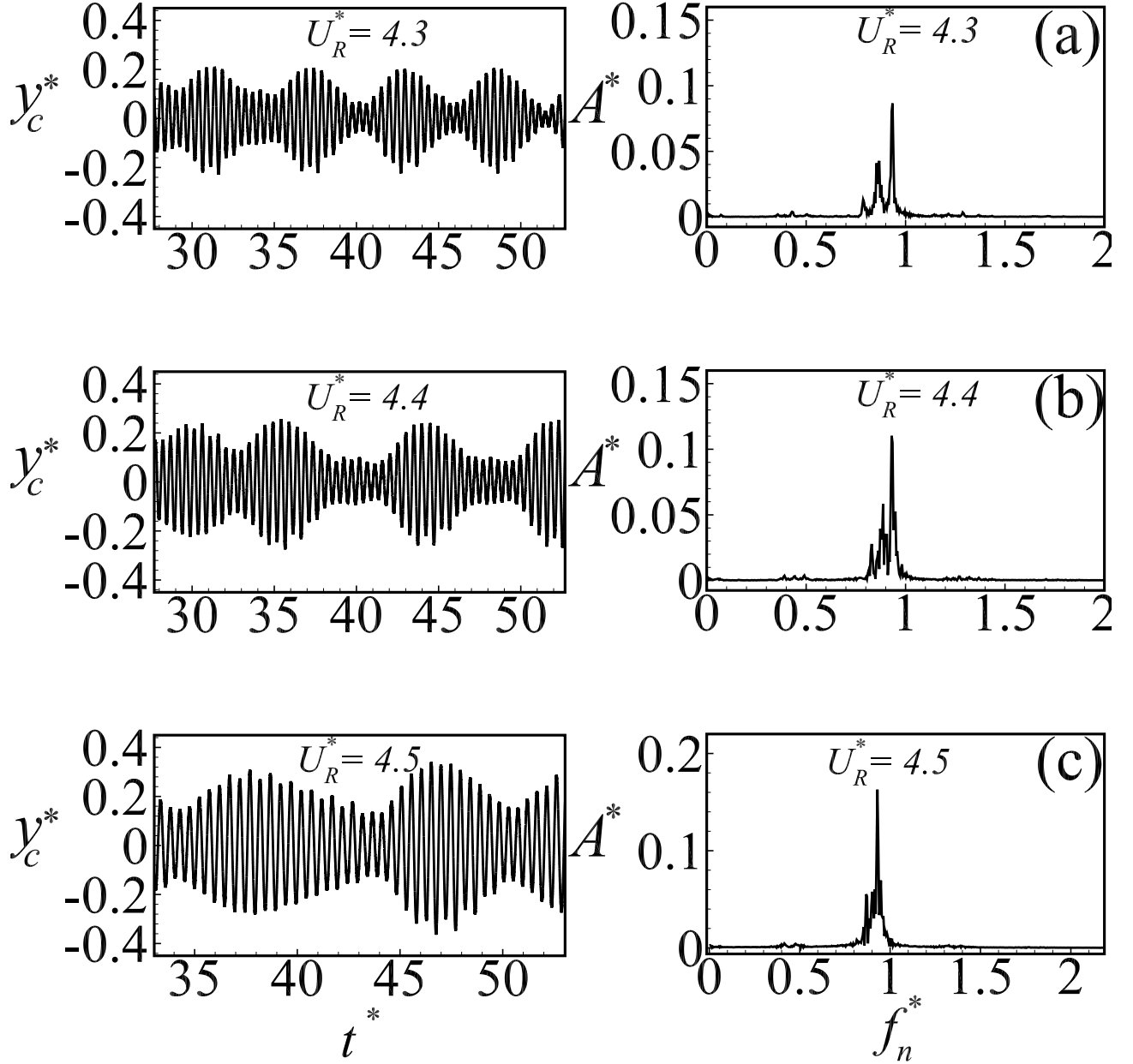
Figure 10: Variation in root-mean-square force coefficients, C_{frms} and C_{lrms}, with reduced velocity U_R^* for KC $= 10$ and $m^*\zeta = 0.01$.
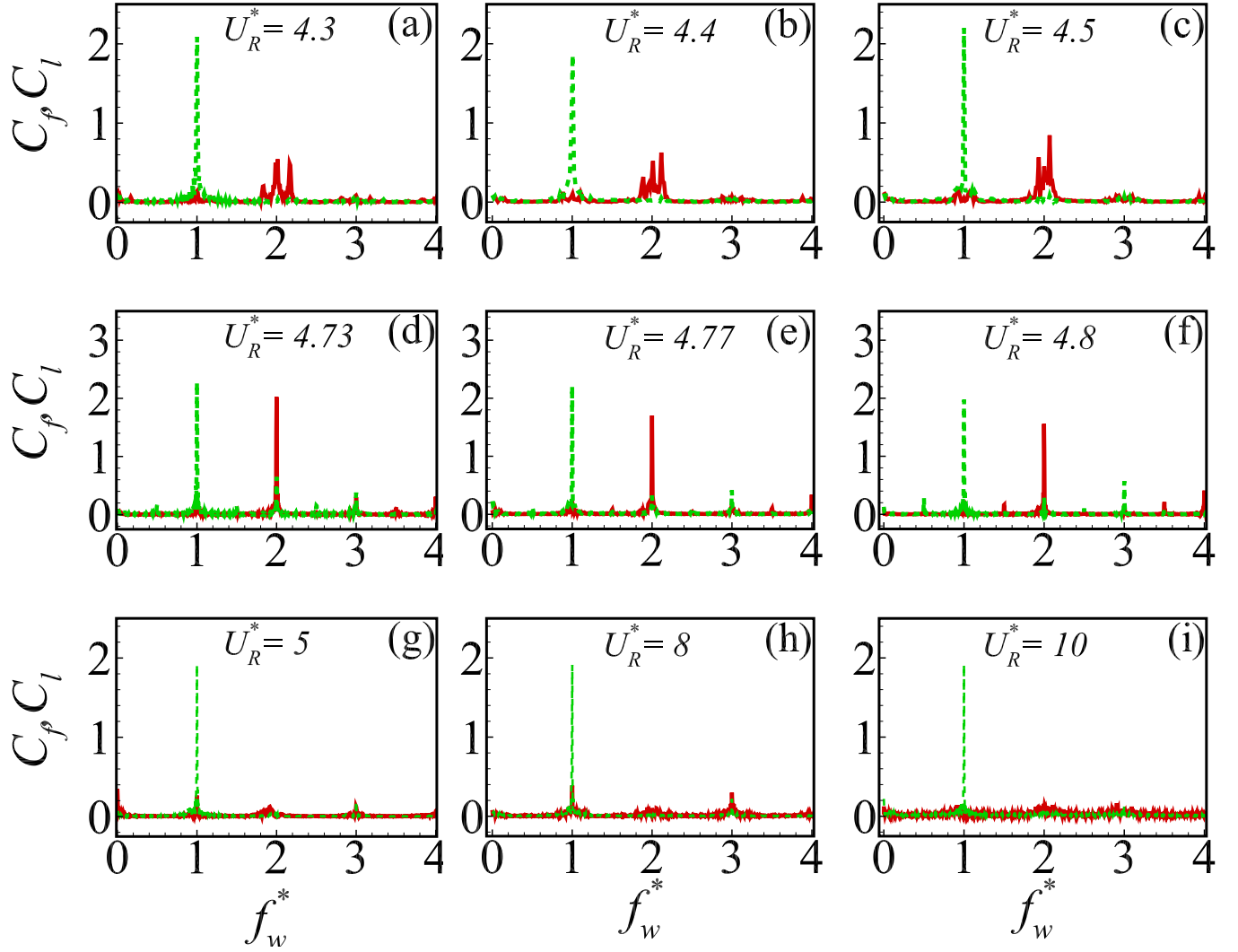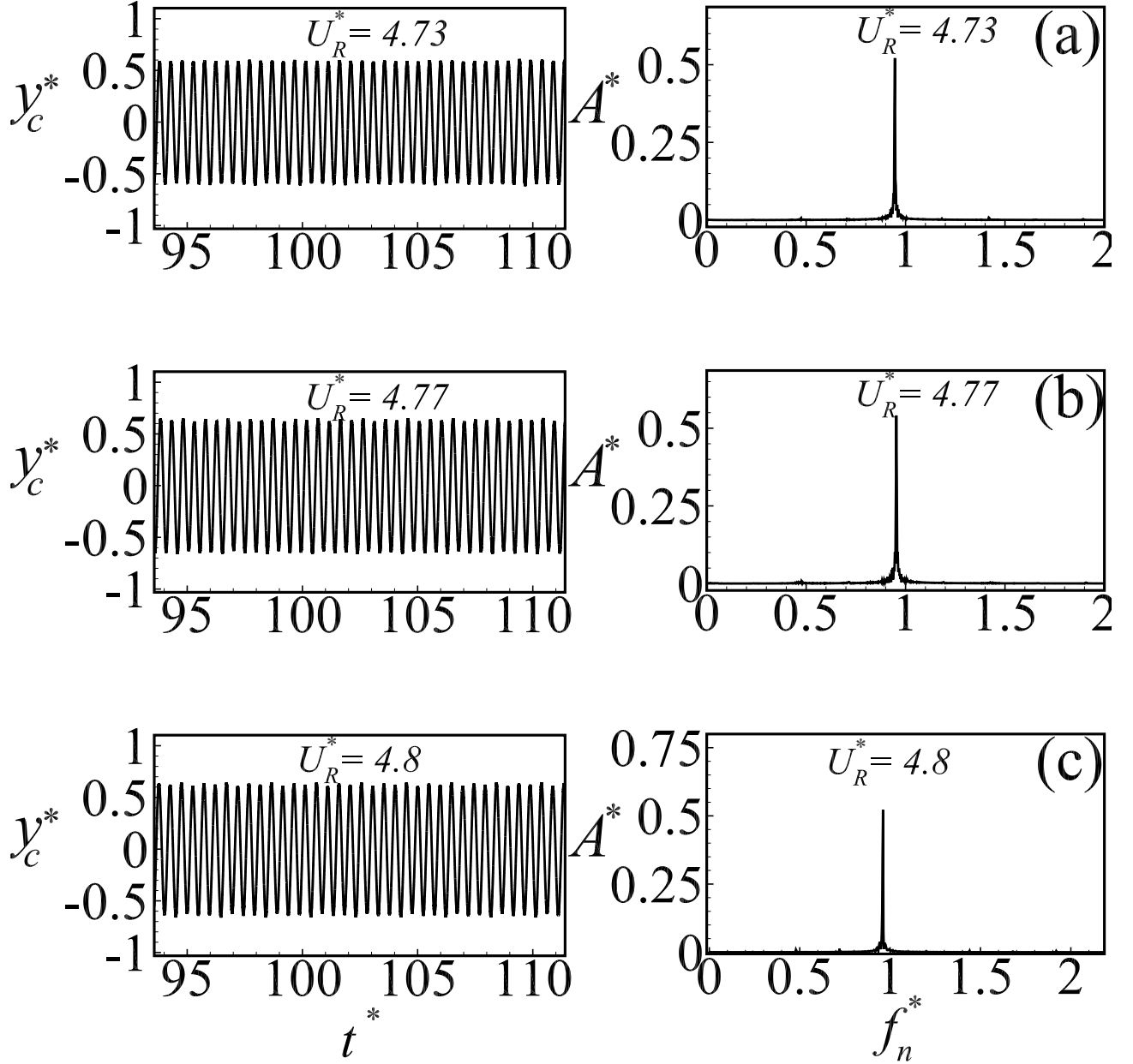
Figure 11: Frequency spectra of inline (C_f – – –) and transverse (C_l ———) force coefficients for KC = 10 and $m^*\zeta = 0.01$: (a) $U_R^* = 4.3$; (b) $U_R^* = 4.4$; (c) $U_R^* = 4.5$; (d) $U_R^* = 4.73$; (e) $U_R^* = 4.77$; (f) $U_R^* = 4.8$; (g) $U_R^* = 5$; (h) $U_R^* = 8$; (i) $U_R^* = 10$.
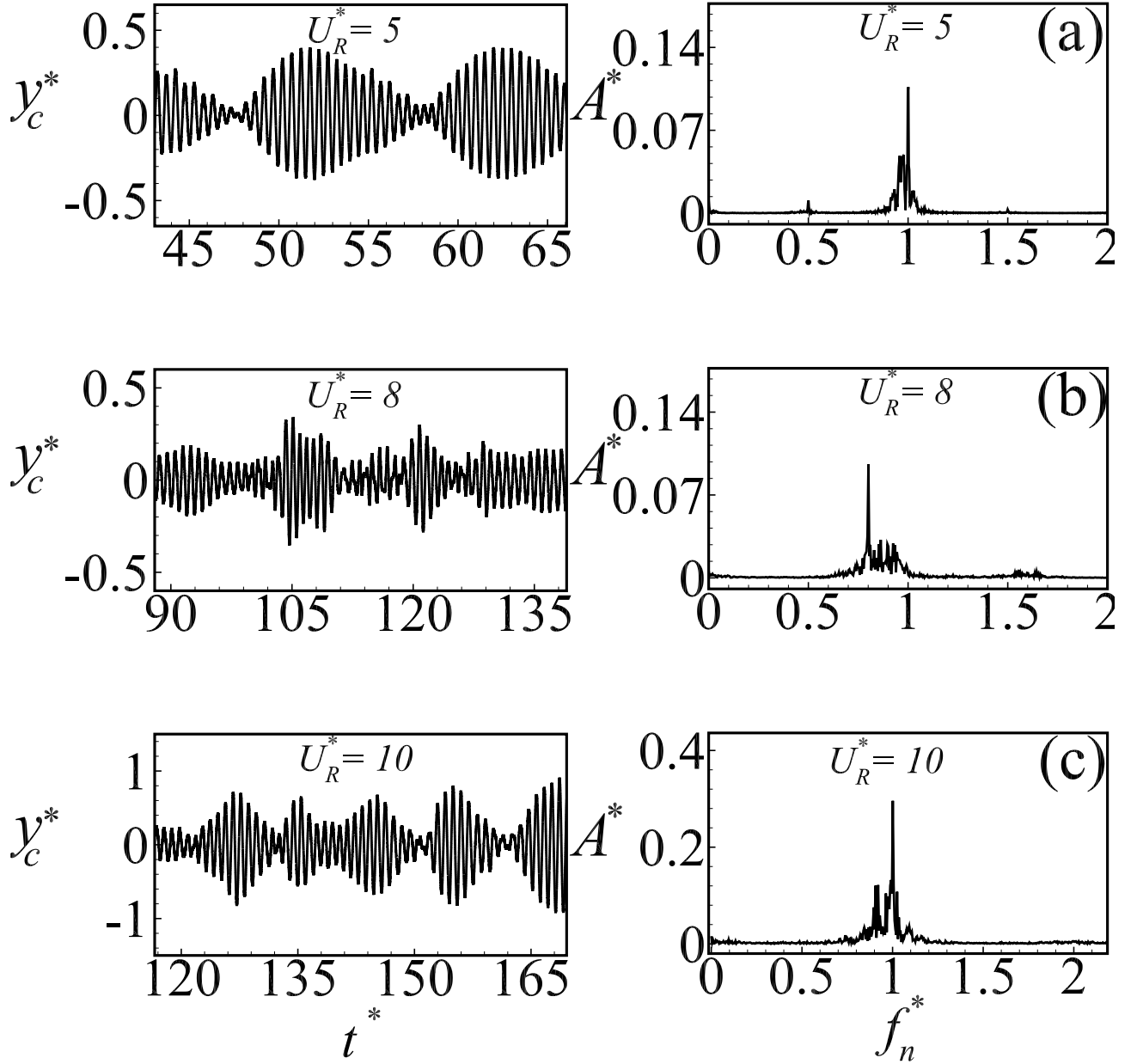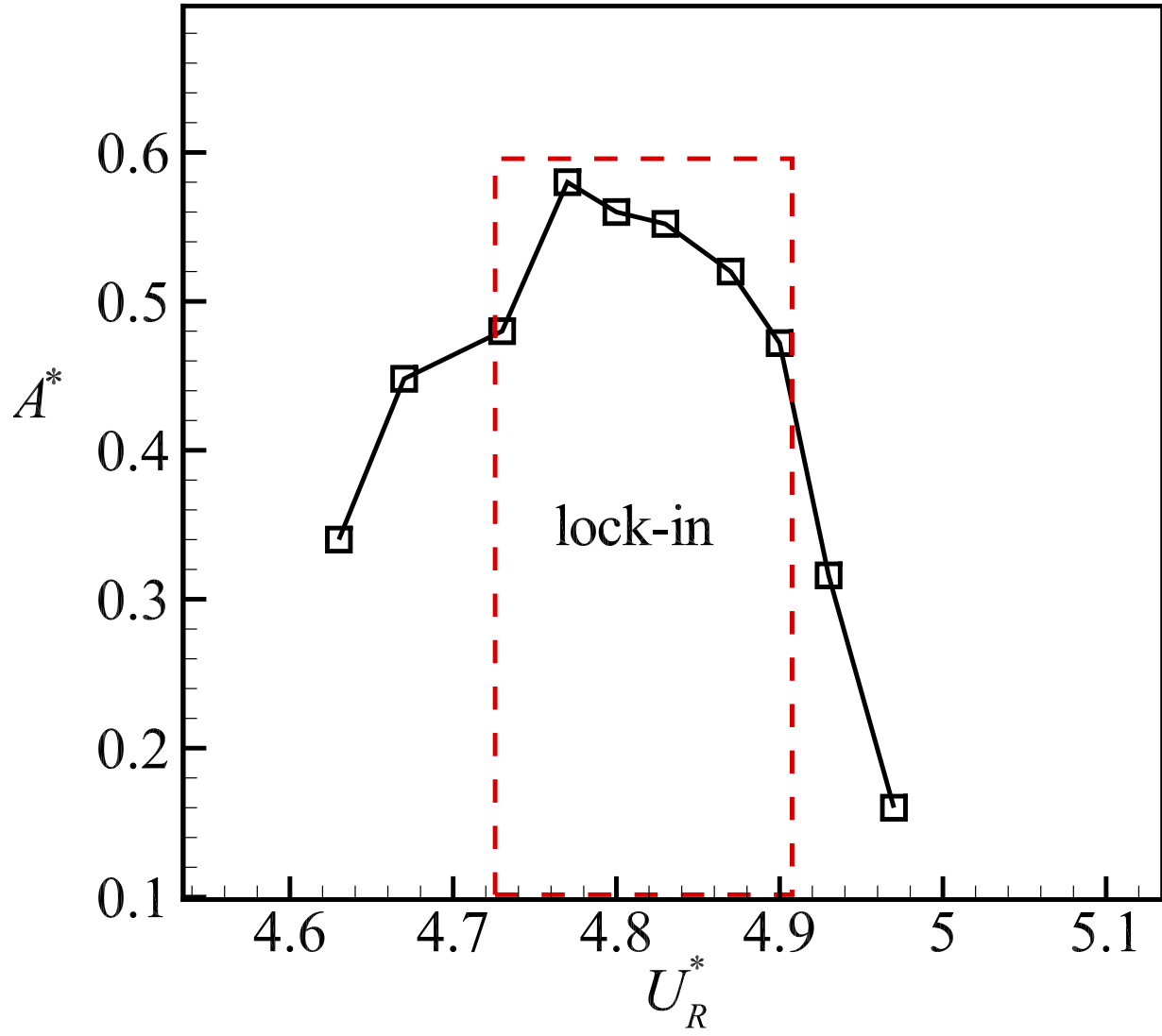
Figure 12: Cylinder non-dimensional transverse displacement $y_c^* = y_c/D$ time series and corresponding frequency response spectrum for KC = 10 and $m^*\zeta = 0.01$ covering the lower beating mode: (a) $U_R^* = 4.3$; (b) $U_R^* = 4.4$; and (c) $U_R^* = 4.5$.

Figure 13: Cylinder non-dimensional transverse displacement $y_c^* = y_c/D$ time series and corresponding frequency response spectrum for KC = 10 and $m^*\zeta = 0.01$ covering the lock-in mode: (a) $U_R^* = 4.73$; (b) $U_R^* = 4.77$; and (c) $U_R^* = 4.8$.

Figure 14: Cylinder non-dimensional transverse displacement $y_c^* = y_c/D$ time series and corresponding frequency response spectrum for KC $= 10$ and $m^*\zeta = 0.01$ covering the upper beating mode: (a) $U_R^* = 5$; (b) $U_R^* = 8$; and (c) $U_R^* = 10$.

Figure 15: Variation in non-dimensional transverse amplitude response $A^* = A/D$ with reduced velocity for KC $= 10$ and $m^*\zeta = 0.01$.